Designing Test Targets for Verification of an Inverse Source Solver at Low Frequencies

Berke Karakin
Technical University of Munich
TUM School of Computation, Information and Technology
Chair of High-Frequency Engineering
Munich, July 1, 2024

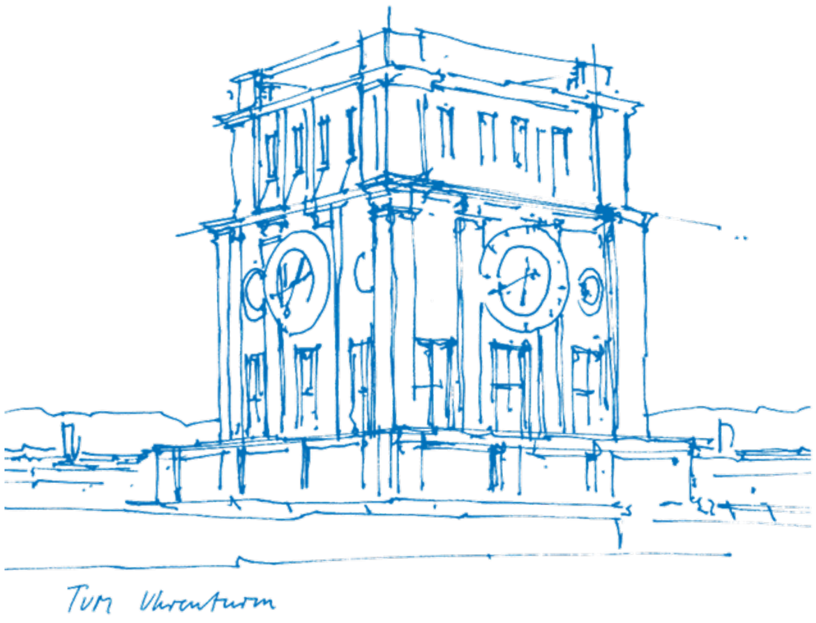

Contents

Introduction

Inverse source solvers are computational methods used for solving inverse scattering problems [1].

In the context of electromagnetics the solver computes equivalent current distributions that produce the observed fields from a set of measurement samples [2].

The solver can then perform important computations such as near-field to near-field or far-field transformations [2].

Some numerical techniques for solving inverse scattering problems based on integral equations suffer from a low frequency breakdown [3].

The goal of this work is to design test circuits with diverse near-field patterns for evaluating the low frequency breakdown of an inverse source solver.

Component Modeling

SMD Inductors

Equivalent Circuit

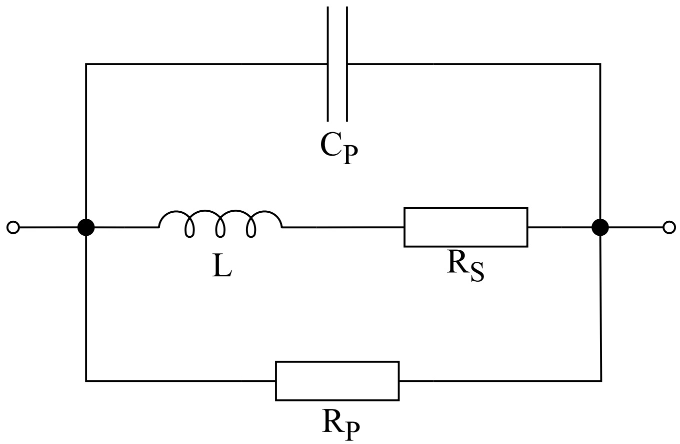

Figure: Equivalent circuit diagram of inductors in Spice simulators.

In the above circuit R_S models the DC resistance of the coil, R_P models losses due to a magnetic core, and C_P models the capacitive coupling between the windings, as well as the coupling between the windings and both the shield and the core.

Self resonance frequency of the inductor:

$$f_{SR} = \frac{1}{2\pi\sqrt{LC_P}} \tag{1}$$

SMD Inductors - Air Core Inductors

Modeling of 744912210 Aircore Inductor by Würth Elektronik

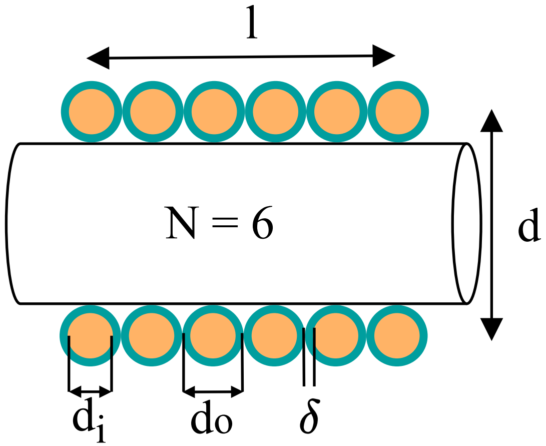

Figure: Geometry parameters of a single layer air core inductor.

The geometry parameters are predicted using the inductance formula for single layer short coils:

$$L_s = N^2 \mu_0 \frac{\pi (d/2)^2}{l} k \,, \tag{2}$$

whereas k is the Nagaoka correction factor [4] and calculated with

$$k = \frac{4}{3\pi} \frac{1}{\kappa'} \left(\frac{\kappa'^2}{\kappa^2} (K(\kappa) - E(\kappa)) + E(\kappa) - \kappa \right) \,, \quad \text{with} \quad \kappa = \frac{d}{d^2 + l^2} \quad \text{and} \quad \kappa' = \frac{l}{d^2 + l^2} \,. \tag{3}$$

Here $K(\cdot)$ and $E(\cdot)$ are the complete elliptical integrals of the first and second kind, respectively.

SMD Inductors - Air Core Inductors

Applying Rosa's round wire correction, the total inductance becomes:

$$L = L_\mathrm{s} - \mu_0 \frac{d}{2} N (k_\mathrm{s} + k_\mathrm{m}) \,, \tag{4}$$

where k_m and k_s are tabularized in [5]. The DC resistance of the inductor is calculated using

$$R_\mathrm{S} = \rho \frac{l_\mathrm{w}}{\pi (d/2)^2} \,, \quad \text{with wire length} \quad l_\mathrm{w} = N \sqrt{(\pi d)^2 + (l/N)^2} \,, \tag{5}$$

and the parasitic resistance of the inductor is calculated using Medhurst's empirical equation in [6]:

$$C_\mathrm{P} = \frac{4 \varepsilon_0 l}{\pi} \left(1 + 0.71 \frac{d}{l} + 2.4 \left(\frac{d}{l} \right)^{1.5} \right) . \tag{6}$$

The feasibility of the predicted geometry is checked using (5), (6) by comparing the results to the manufacturer's data. Subsequently a valid coil geometry is decided.

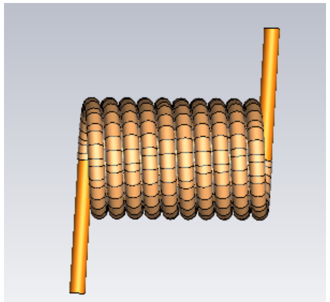

Figure: 3D model of the air core inductor 744912210 in CST.

SMD Inductors - Air Core Inductors

N	d (mm)	l (mm)	d_{i} (mm)	δ (mm)
10	2.6	4.5	0.4	0.0185

Table: Valid geometry from the analytical equations for the air core inductor 744921210.

Model number	Results from	$L\,(\mathrm{nH})$	$R_{\mathrm{S}}\,(\mathrm{m}\Omega)$	$C_{\mathrm{P}}\,(\mathrm{pF})$	$f_{\mathrm{SR}}\,(\mathrm{GHz})$
744912210	Equations	105	12.1	0.125	1.390
	CST	100	12.8	0.131	1.389
	Datasheet	$100 \pm 5\%$	< 12.3	< 0.176	> 1.2

Table: Important values obtained from analytical equations and from CST are compared with the data provided by the manufacturer for the air core inductor 744912210.

SMD Inductors - Important Ferrite Core Concepts

Effective relative permeability

For open cores the ratio between the inductance with and without a ferrite core ($L_f/L_{air} =: \mu_{r,eff}$) can be much lower than the relative permeability μ_r of the core, depending on the core geometry. In [7] following formula is introduced for calculating $\mu_{r,eff}$:

$$\mu_{r,eff} = \frac{\mu_r}{1 + D(\mu_r - 1)}, \tag{7}$$

where D is the demagnetization factor. For cylindrical rods it is given in the graphs below.

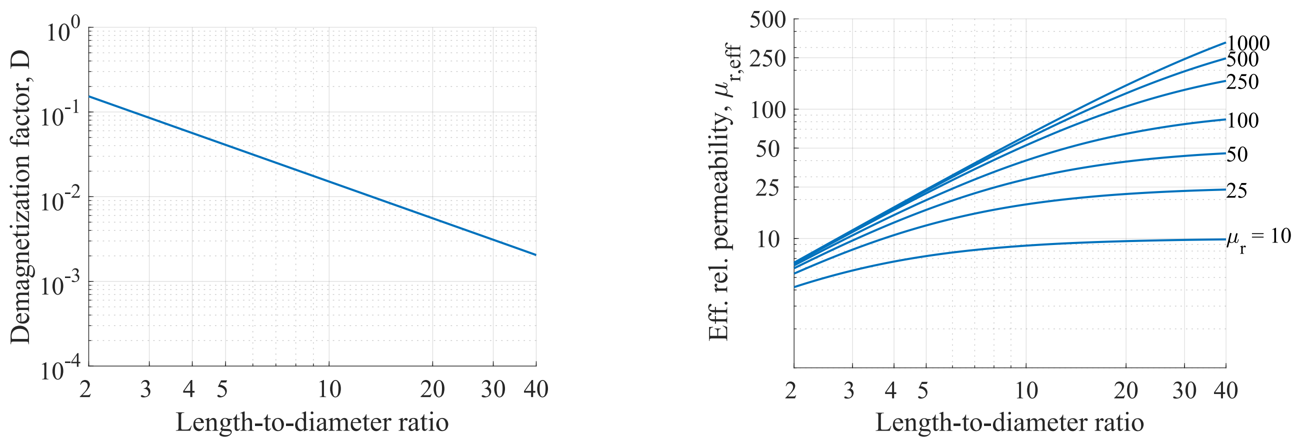

Figure: Demagnetization factor of a cylindrical core depending on the length-to-diameter ratio (left). Eff. rel. permeability $\mu_{r,eff}$ of a cylindrical magnetic core depending on the relative permeability and the length-to-diameter ratio (right).

SMD Inductors - Important Ferrite Core Aspects

Core saturation

In the equation

$$\vec{B} = \mu_0 \vec{H} + \mu_0 \vec{M} \tag{8}$$

the contribution of $\mu_0 \vec{M}$ stops increasing for very large $\vec{H}$ and μ_r drops to 1.

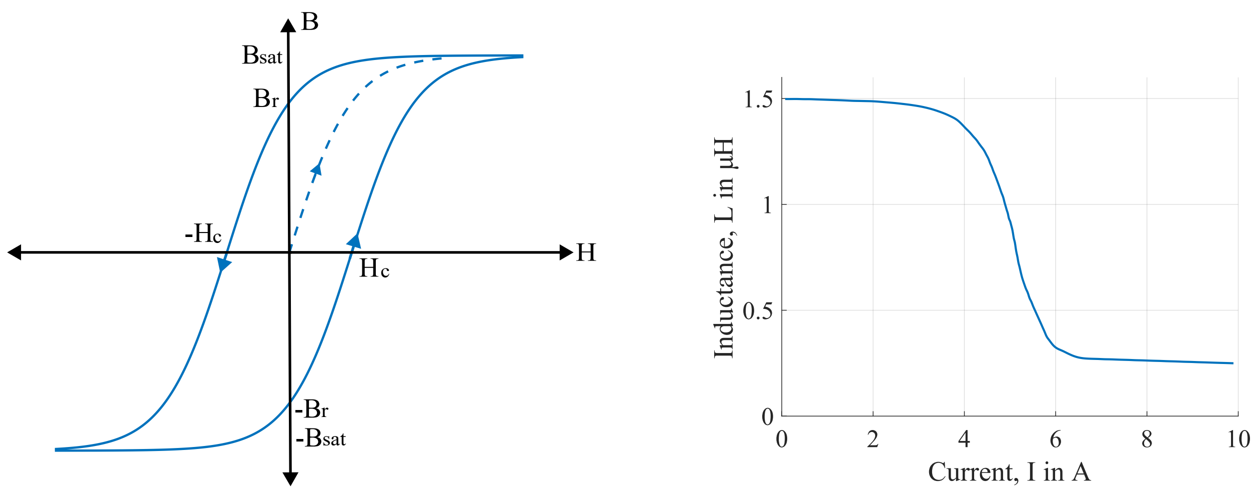

Figure: Qualitative magnetization curve for an arbitrary magnetic core (left). Inductance of 7440450015 drum core inductor from Würth Elektronik depending on the current (right).

SMD Inductors - Important Ferrite Core Aspects

Dispersion of relative permeability

$$\underline{\mu}_{\mathrm{r}}(\omega) = 1 + \underline{\chi}_{\mathrm{sp}}(\omega) + \underline{\chi}_{\mathrm{dw}}(\omega)\,, \tag{9}$$

$$\underline{\mu}_{\mathrm{r}}(\omega) = 1 + \frac{(\omega_{\mathrm{sp}} + j\omega\alpha)\,\omega_{\mathrm{sp}}\chi^0_{\mathrm{sp}}}{(\omega_{\mathrm{sp}} + j\omega\alpha)^2 - \omega^2} + \frac{\omega^2_{\mathrm{dw}}\chi^0_{\mathrm{dw}}}{\omega^2_{\mathrm{dw}} - \omega^2 + j\omega\beta}\,, \quad \text{for } \alpha \gg 1,\ \underline{\chi}_{\mathrm{sp}} \text{ becomes } \frac{\chi^0_{\mathrm{sp}}}{1 + j\omega\tau}\,, \tag{10}$$

where χ^0_{sp}, χ^0_{dw} are low frequency susceptibilities of spin rotation and domain wall motion, ω_{sp}, ω_{dw} are the corresponding resonance frequencies, α, β are damping factors and τ is the relaxation time constant [8]–[10].

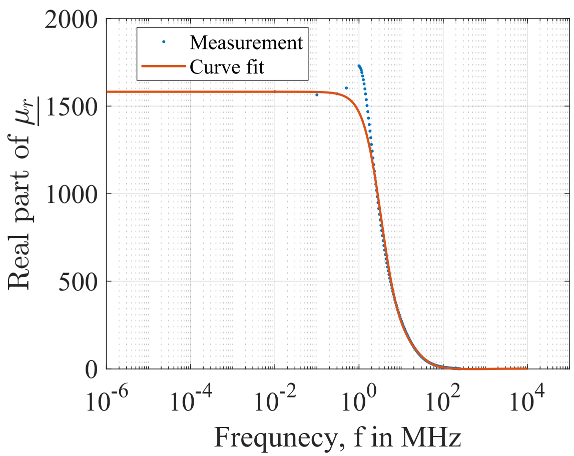

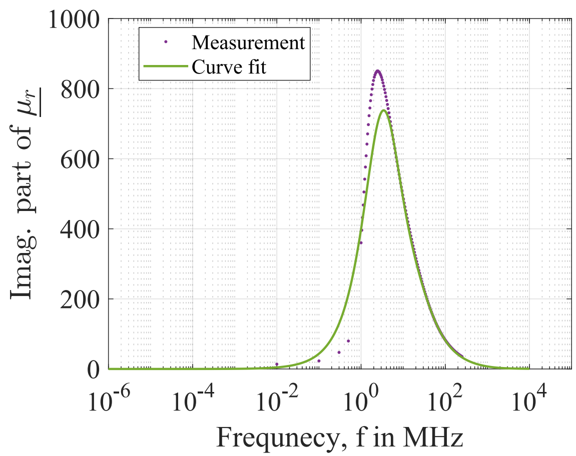

Figure: Complex permeability of the Fair-Rite 15 Material is fitted with (10). The following parameters are obtained from the particle swarm optimizer in MATLAB: $\chi^0_{\mathrm{sp}} = 1433$, $\omega_{\mathrm{sp}} = 9 \times 10^9\,\mathrm{rad/s}$, $\alpha = 427.7$; $\chi^0_{\mathrm{dw}} = 147$, $\omega_{\mathrm{dw}} = 1.1 \times 10^9\,\mathrm{rad/s}$, $\beta = 8.3 \times 10^9\,\mathrm{rad/s}$

SMD Inductors - Drum Core Inductors

Modeling of 7440450015 and 744045002 drum core inductors from Würth Elektronik.

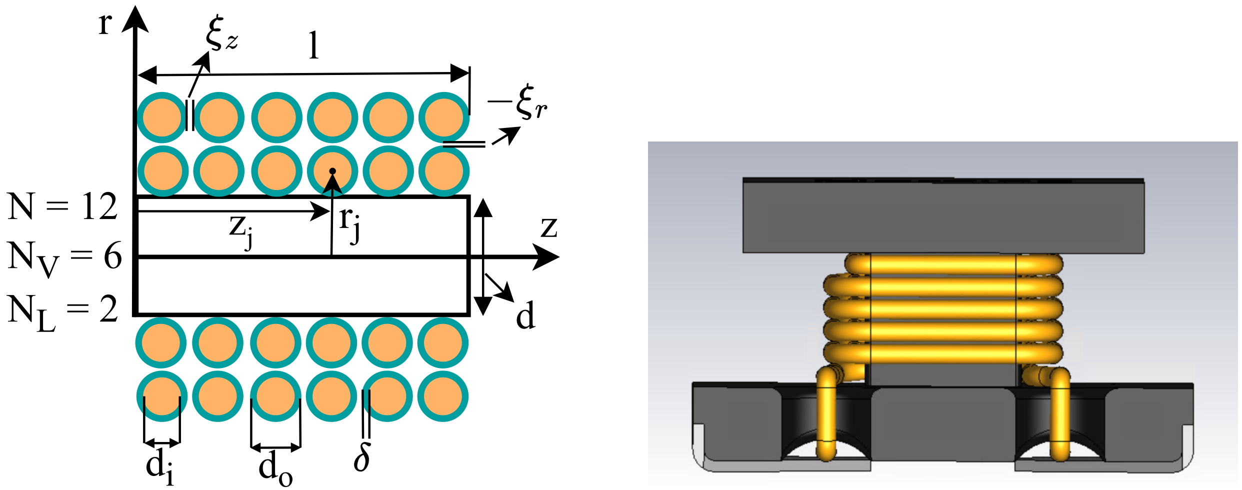

Figure: Geometry parameters of multilayer inductors (left). 3D CAD model of 744045001 from Würth Elektronik (right).

In the first step, the core is ignored. The multilayer coil is modeled similar to [11]. The geometry parameters of the coil is predicted using

$$L_{\text{air}} = \sum_{j=0}^{N} L_j + \sum_{j=0}^{N} \sum_{\substack{k=0 \\ k \neq j}}^{N} M_{jk}\,, \tag{11}$$

whereas L_j is the self-inductance of the j-th winding and M_{jk} is the mutual inductance between the j-th and k-th windings and L_{air} is taken from the inductance vs.current graphs in datasheets [11].

SMD Inductors - Drum Core Inductors

From Grover's book [12], for a square winding with side length r_j and wire radius $d_i/2$, the self inductance is

$$L_j = \mu_0 \frac{2r_j}{\pi} \left(\ln\left(\frac{2r_j}{(d_i/2)} \right) - 0.77401 \right). \tag{12}$$

and from Cheng and Shu's paper [13], for two coaxial square current filaments with side lengths $2a$ and $2c$ and distance apart z, the mutual inductance is

$$\begin{aligned} M = \frac{2\mu_0}{\pi} \Bigg[& \sqrt{2(a+c)^2+z^2} + \sqrt{2(a-c)^2+z^2} - 2\sqrt{2a^2+2c^2+z^2} \\ & - (a+c)\,\mathrm{arctanh}\left(\frac{a+c}{\sqrt{2(a+c)^2+z^2}} \right) - (a-c)\,\mathrm{arctanh}\left(\frac{a-c}{\sqrt{2(a-c)^2+z^2}} \right) \\ & + (a+c)\,\mathrm{arctanh}\left(\frac{a+c}{\sqrt{2a^2+2c^2+z^2}} \right) + (a-c)\,\mathrm{arctanh}\left(\frac{a-c}{2a^2+2c^2+z^2} \right) \Bigg]. \end{aligned} \tag{13}$$

To make this equation compatible with the model used in this work and thus to obtain M_{jk}, a needs to be replaced with r_j, c needs to be replaced with r_k, and z needs to be replaced with $|z_j - z_k|$.

SMD Inductors - Drum Core Inductors

The DC resistance of a multilayer coil can be calculated with

$$R_\mathrm{S} = \rho_\mathrm{c} \frac{l_\mathrm{w}}{\pi (d_\mathrm{i}/2)^2}, \quad \text{with} \quad l_\mathrm{w} = \sum_{j=0}^{N} \left(4\sqrt{(2r_j)^2 + (p/4)^2} \right), \tag{14}$$

where $p = d_\mathrm{o} + \xi_z$ is the pitch of the windings.

Finally the inductors are implemented in CST. The relative permeabilities are determined with a parameter sweep. The dispersion had to be modeled with the 1st order Debye model and the parameter τ is optimized such that the parallel resistances R_P match together.

Inductor	L_f (µH)	L_air (µH)	μ_r	$\mu_\mathrm{r,eff}$	D	τ (ns)	N	N_L	N_V
7440450015	1.50	0.216	22	6.94	0.11	0.95	12	2	6
744045002	2.23	0.333	25	6.67	0.11	0.65	15	3	5

Inductor	l (mm)	d (mm)	d_i (mm)	δ (mm)	d_o (mm)	ξ_z (mm)	ξ_r (mm)
7440450015	1.08	1.4	0.16	0.01	0.18	0.005	-0.005
744045002	1.00	1.4	0.18	0.01	0.20	0.005	-0.005

Table: Geometry parameters as well as material parameters predicted for 7440450015 and 744045002.

SMD Inductors - Drum Core Inductors

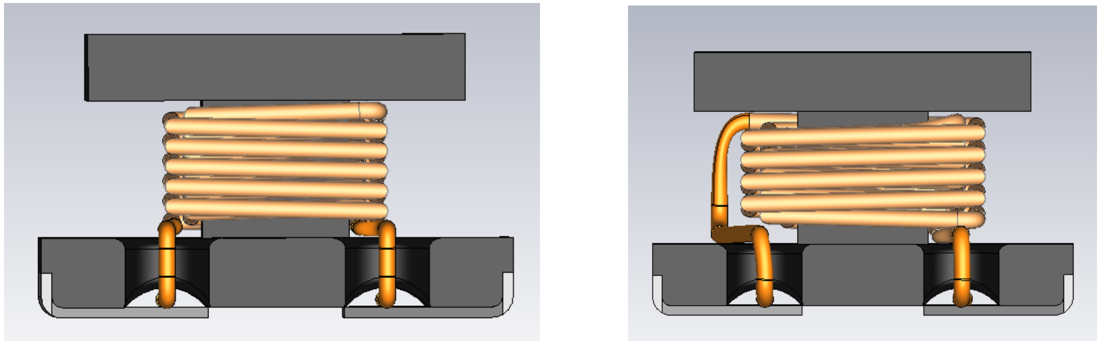

Figure: 3D models of the inductors in CST. 7440450015 on the left and 744045002 on the right.

Model number	Results from	L_f (µH)	L_{air} (µH)	R_S (Ω)	R_P (Ω)	C_P (pF)	f_{SR} (MHz)
7440450015	Equations	–	0.229	0.073	–	–	–
	CST	1.5	0.216	0.077	3330.8	0.834	145
	LTSpice	1.5	–	0.072	3303.9	1.155	121
	Datasheet	$1.5 \pm 20\%$	0.235	< 0.090	–	≈ 1	≈ 130
744045002	Equations	–	0.404	0.082	–	–	–
	CST	2.23	0.333	0.086	8002.9	0.72	123
	LTSpice	2.2	–	0.088	7826.2	0.863	120
	Datasheet	$2.2 \pm 20\%$	0.32	< 0.110	–	≈ 1.8	≈ 80

Table: Important results from analytical equations and from CST simulations are compared with the data provided by the manufacturer, taken from the datasheets and the Spice models.

SMD Inductors - Drum Core Inductors

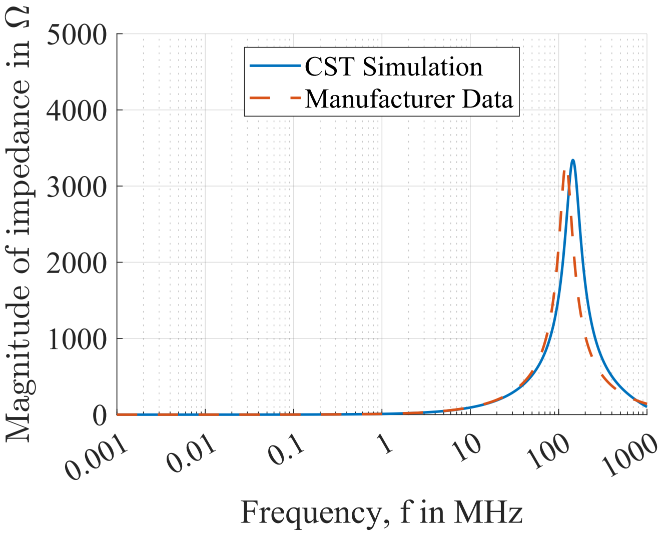

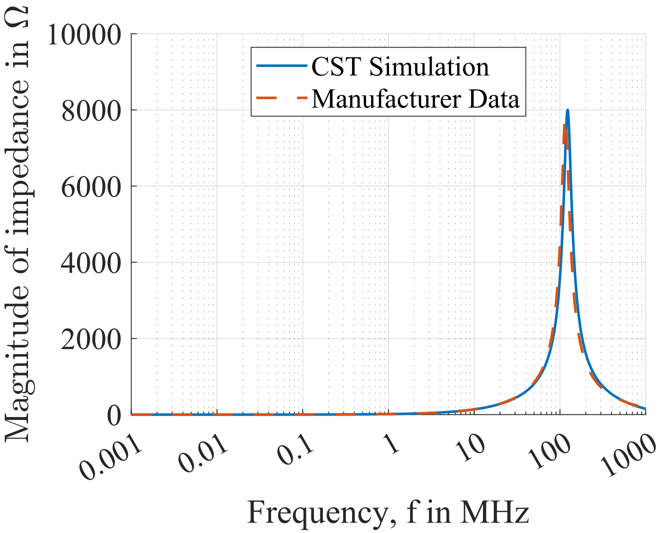

Figure: Comparison between the $|\underline{Z}_{\mathrm{L}}(\omega)|$ values from CST and simulation of manufacturer's Spice model for 7440450015 (left) and for 744045002 (right).

SMD Capacitors

Inner structure and equivalent circuit

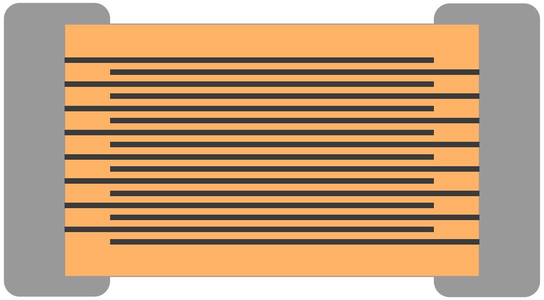

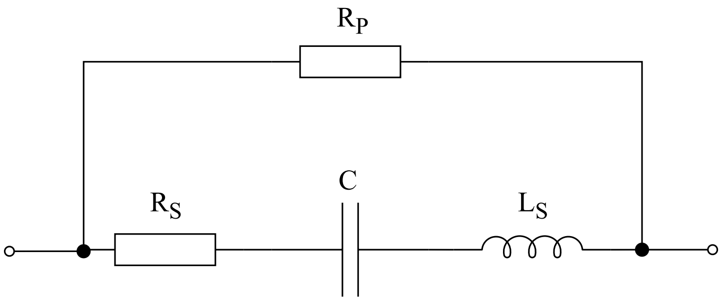

Figure: Inner structure of a multi-layer ceramic capacitor (MLCC) (left) and its equivalent circuit in Spice simulators (right).

An MLCC consists of stacked metal layers in a ceramic dielectric. Adjacent metal layers are connected to opposite electrodes, forming a parallel connection so that total capacitance becomes $N_C \varepsilon_0 \varepsilon_r A/d$, where N_C is the number of layers [14].

In the equivalent circuit above R_S models the losses in the dielectric, R_P models the current leakage through the dielectric and L_S models the inductance of metal connections.

SMD Capacitors

3D modeling

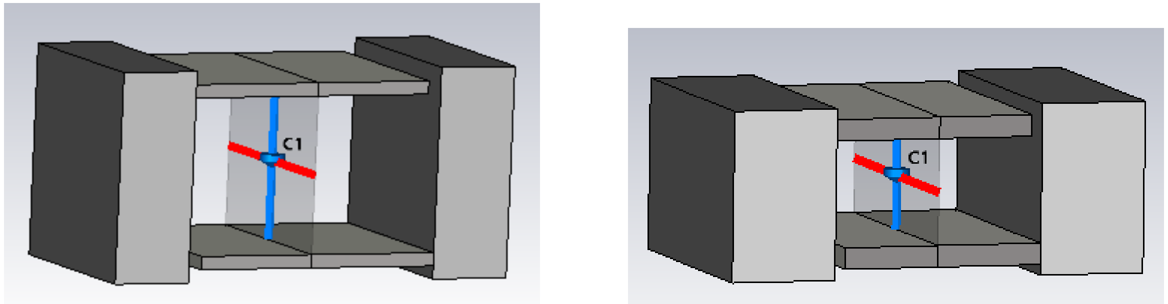

Figure: Two examples out of various capacitor models implemented in CST. 885342008003 (left) and 885012007087 (right).

For the 3D modeling of MLCCs the brick modeling approach is followed in accordance with Modelithics and [15].

The external geometry of the component is exact. The internal part of the component contains a lumped element that includes the manufacturer-released Spice model.

SMD Resistors

Inner structure, equivalent circuits and 3D modeling

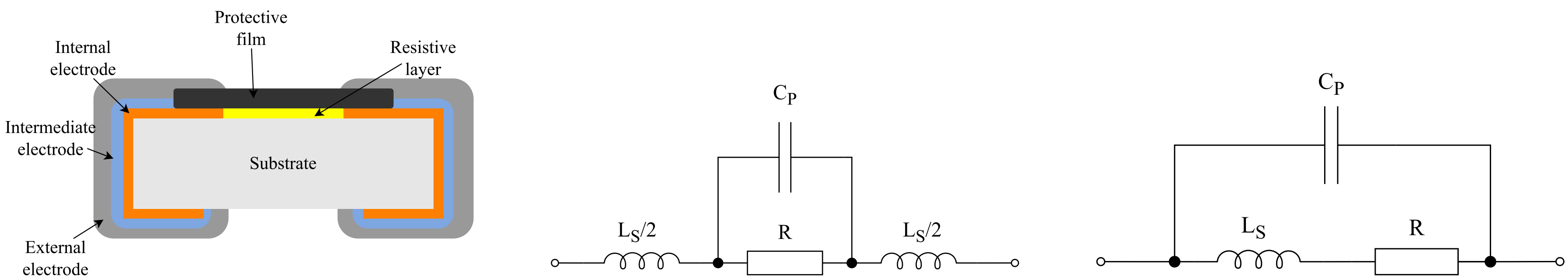

Figure: Inner structure of a thin-/thick-film resistor (left), its equivalent circuit for $R \lessapprox 100\,\Omega$ (middle) and for $R \gtrapprox 100\,\Omega$ (right) [16]

The impedance of the resistor in the middle continuously increases with increasing frequency, whereas the impedance of the resistor on the left contentiously decreases.

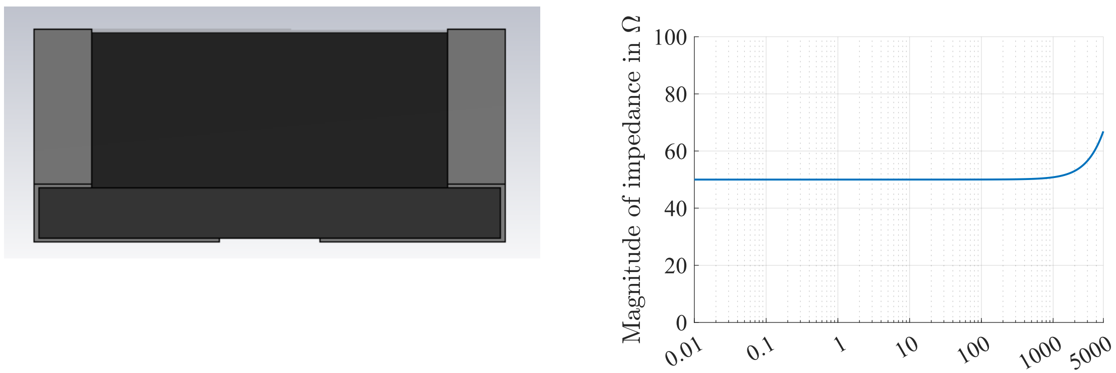

Figure: The $50\,\Omega$ resistor RCP1206W50R0GEB modeled in CST (left) and its impedance depending on the frequency (right).

Circuit Implementations

Loop Circuit

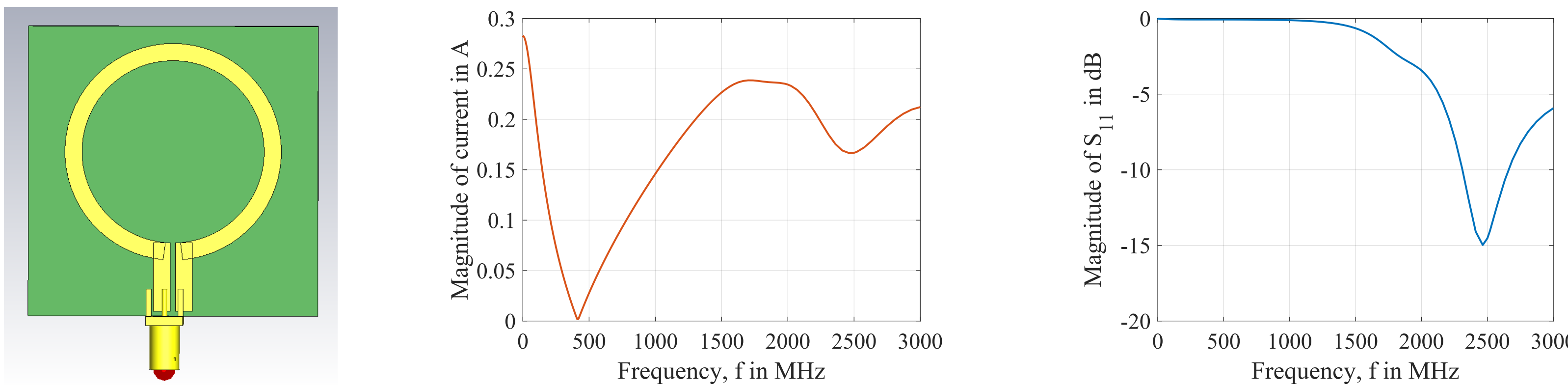

Figure: Loop circuit implemented in CST (left), the magnitude of current through it (middle) and magnitude of the S_{11}-parameter (right).

The circuit is implemented on a $50.8\,\mathrm{mm} \times 50.8\,\mathrm{mm}$ Rogers RO4003C PCB without a ground plane at the bottom. The inner radius of the loop is $17.5\,\mathrm{mm}$ and the wire width is $3\,\mathrm{mm}$.

Loop Circuit

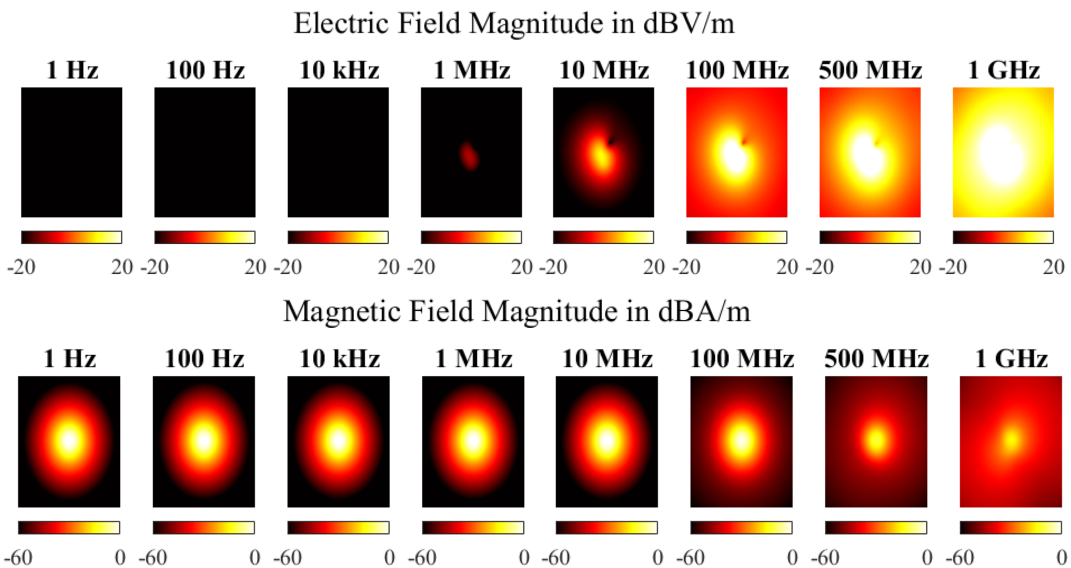

Figure: Near-field simulation results collected 3 cm above the circuit in a 40 cm × 40 cm plane for the loop circuit.

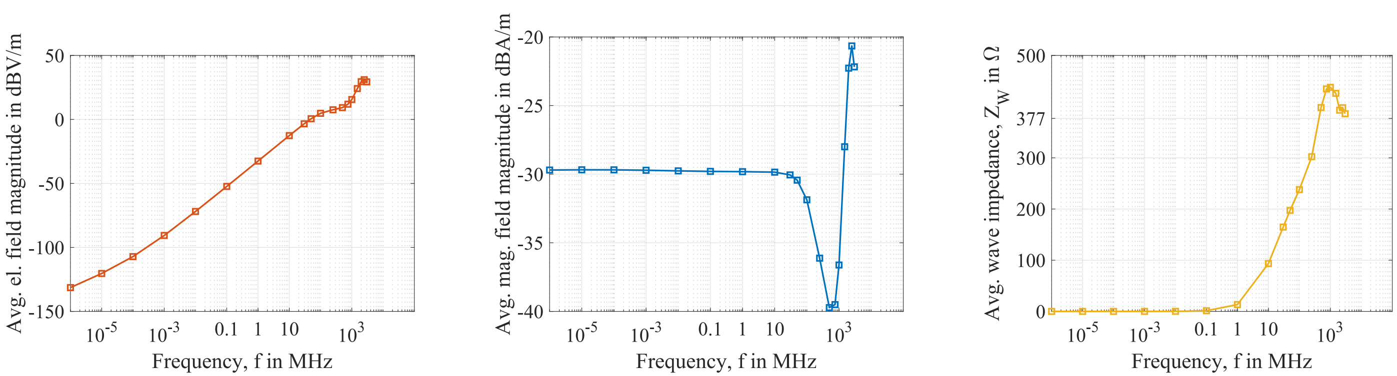

Figure: Field magnitudes and wave impedance averaged in the sampling plane for the loop circuit.

Patch Circuit

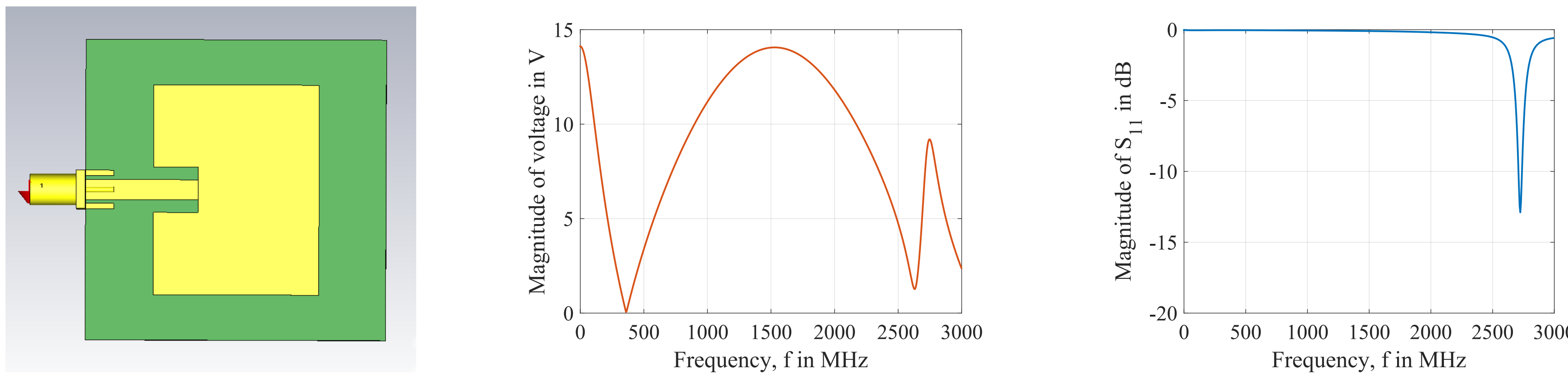

Figure: Patch circuit implemented in CST (left), the magnitude of voltage over it (middle) and magnitude of the S_{11}-parameter (right).

The circuit is implemented on a $50.8\,\mathrm{mm} \times 50.8\,\mathrm{mm}$ Rogers RO4003C PCB with a ground plane at the bottom layer. The patch at the top layer has dimensions $28\,\mathrm{mm} \times 35.5\,\mathrm{mm}$.

Patch Circuit

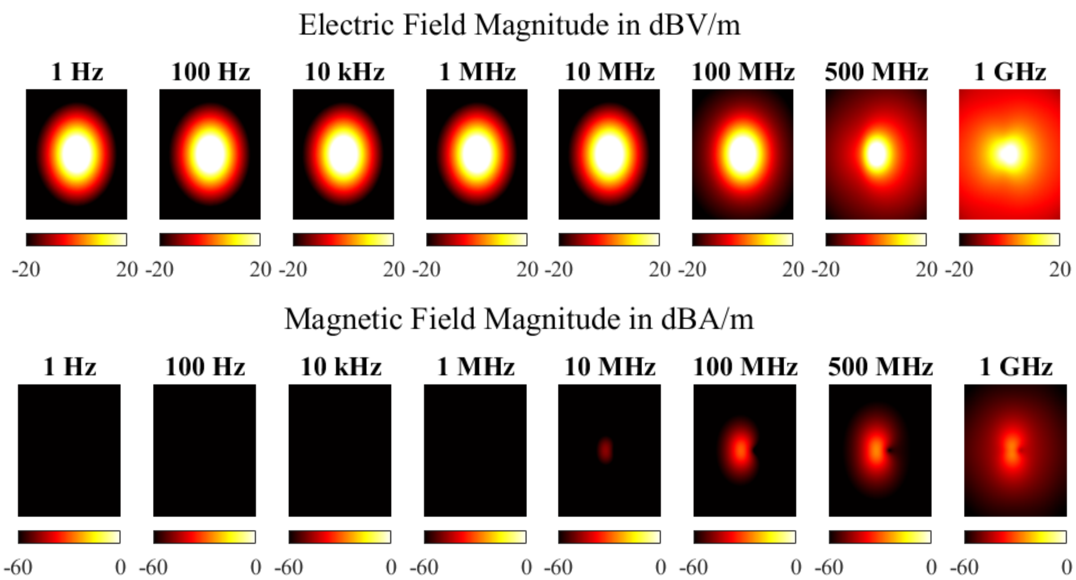

Figure: Near-field simulation results collected 3 cm above the circuit in a 40 cm × 40 cm plane for the patch circuit.

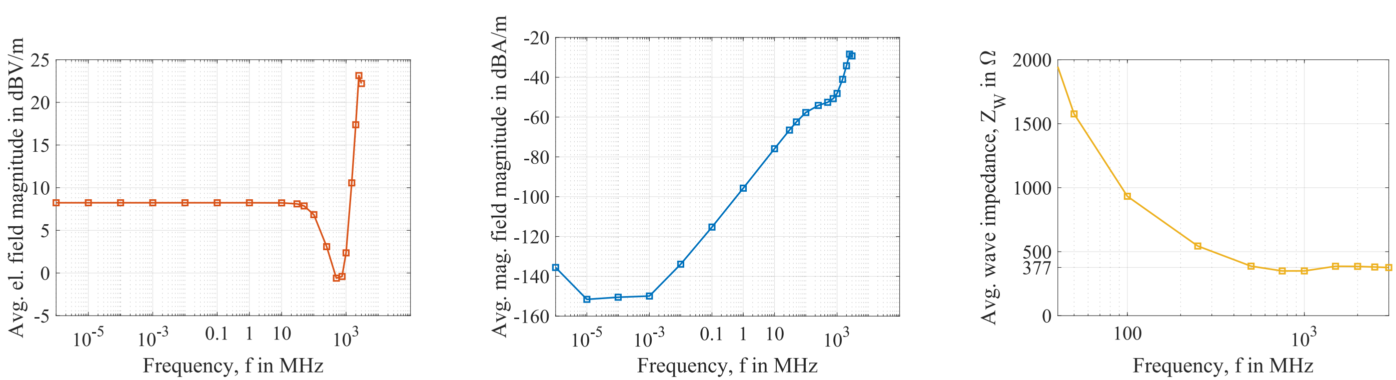

Figure: Field magnitudes and wave impedance averaged in the sampling plane for the patch circuit.

Coplanar Circuit

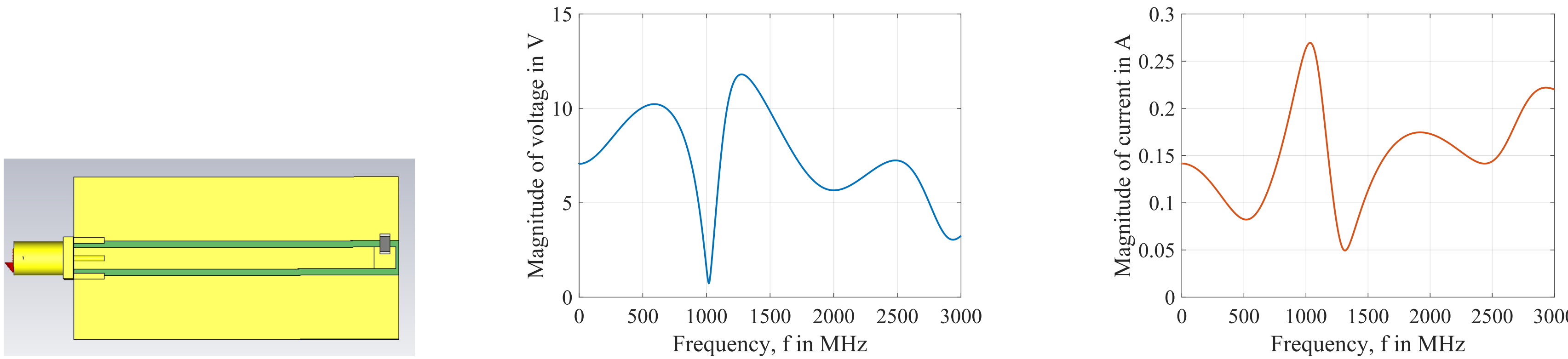

Figure: Coplanar circuit implemented in CST (left), the magnitude of the voltage over it (middle) and magnitude of the current through (right).

The circuit is implemented on a $50.8\,\text{mm} \times 25.4\,\text{mm}$ Rogers RO4003C PCB without a ground plane at the bottom layer.

Coplanar Circuit

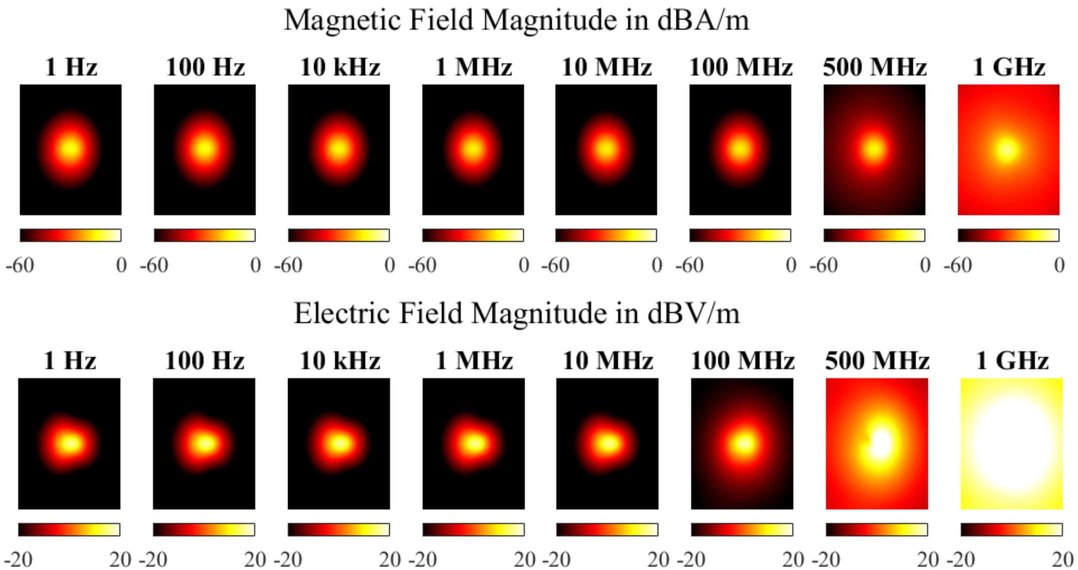

Figure: Near-field simulation results collected 3 cm above the circuit in a 40 cm $\times$ 40 cm plane for the resistor circuit.

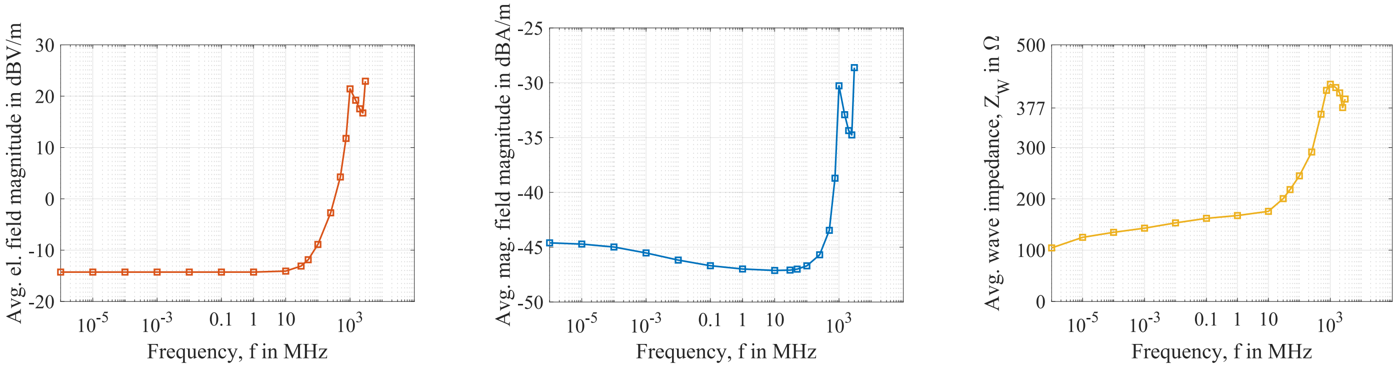

Figure: Field magnitudes and wave impedance averaged in the sampling plane for the resistor circuit.

LC Bandpass Filters

3rd order LC Bandpass filter, 1st variant

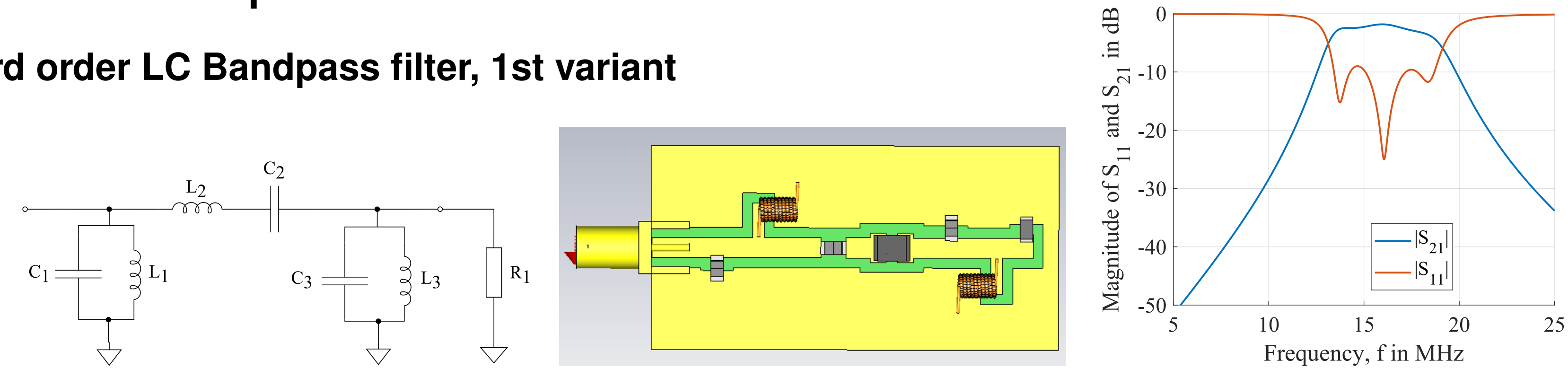

Figure: Bandpass filter's circuit diagram (left), its implementation in CST (middle), and its important S-parameters.

The circuit is implemented on a $50.8\,\mathrm{mm} \times 25.4\,\mathrm{mm}$ Rogers RO4003C PCB with a ground plane at the bottom layer.

–	L_1	C_1	L_2	C_2
Component value	$100\,\mathrm{nH}$	$1\,\mathrm{nF}$	$1.5\,\mu\mathrm{H}$	$68\,\mathrm{pF}$
Model number	744912210	885342008003	7440450015	885342008010

–	L_3	C_3	R_1
Component value	$100\,\mathrm{nH}$	$1\,\mathrm{nF}$	$50\,\Omega$
Model number	744912210	885342008003	RCP1206W50R0GEB

Table: Obtained component values from design equations in [17] rounded to the closest standard value.

LC Bandpass Filters

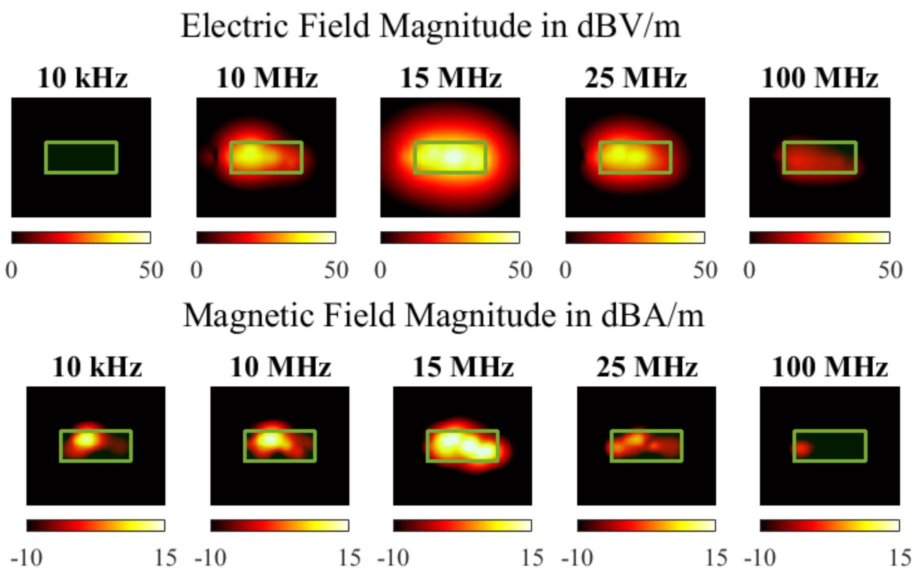

Reminder:

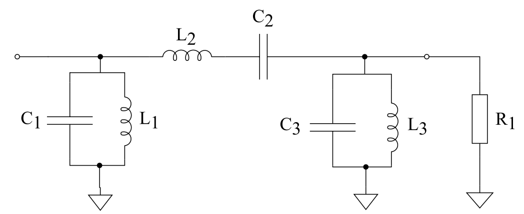

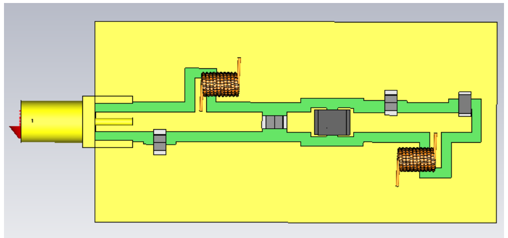

Figure: Near-field simulation results collected 1 cm above the circuit in a 10 cm × 10 cm plane for the bandpass filter.

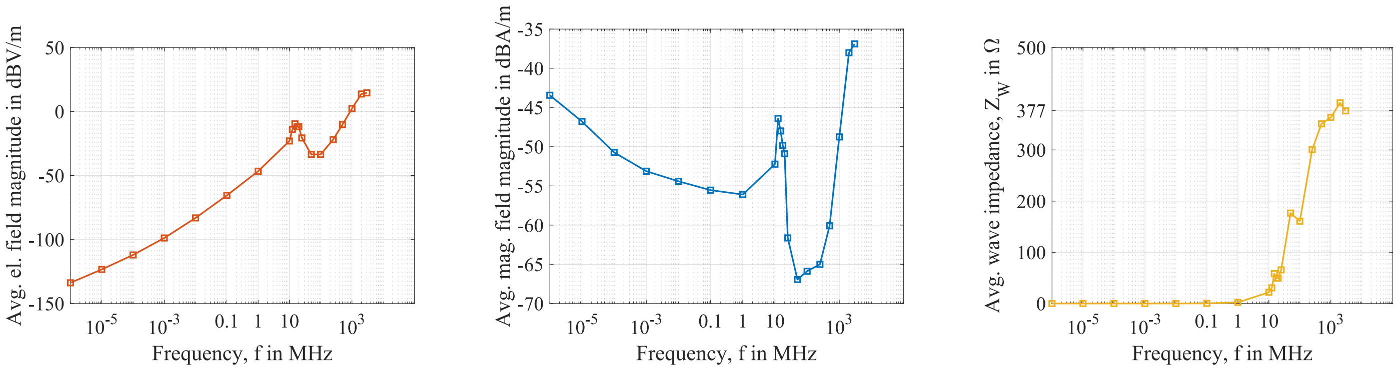

Figure: Average field magnitudes and wave impedance collected 3 cm above the circuit in a 40 cm × 40 cm plane.

LC Bandpass Filters

3rd order LC Bandpass filter, 2nd variant

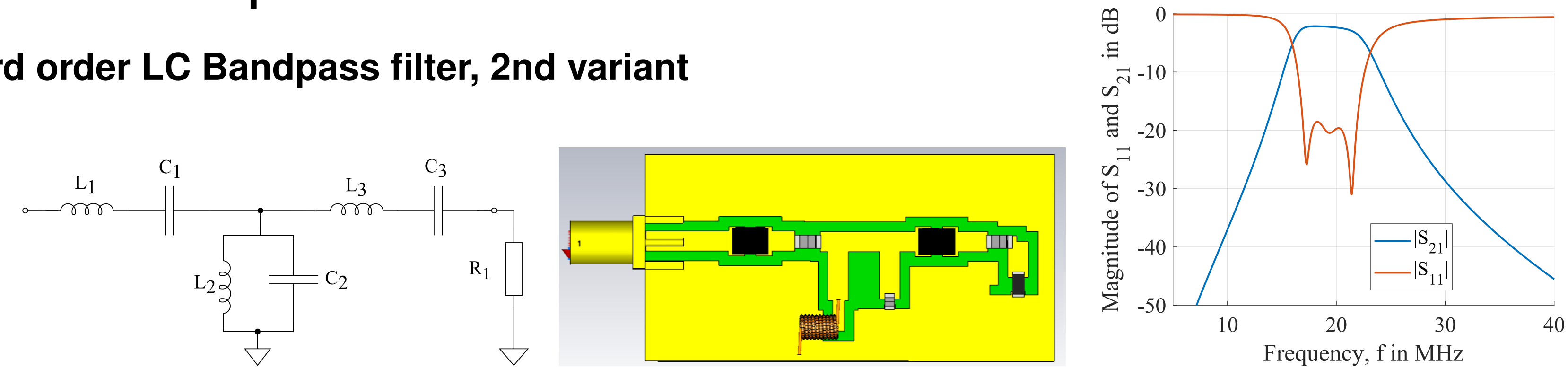

Figure: Circuit diagram (left), filter's implementation in CST (middle), and its important S-parameters.

The circuit is implemented on a $25.4\,\mathrm{mm} \times 50.8\,\mathrm{mm}$ Rogers RO4003C PCB with a ground plane at the bottom layer.

–	L_1	C_1	L_2	C_2
Component value	$1.5\,\mu$H	$47\,$pF	$100\,$nH	$680\,$pF
Model number	7440450015	885342008001	744912210	885012007087

–	L_3	C_3	R_1
Component value	$1.5\,\mu$H	$47\,$pF	$50\,\Omega$
Model number	7440450015	885342008001	RCP1206W50R0GEB

Table: Obtained component values from design equations in [17] rounded to the closest standard value.

LC Bandpass Filters

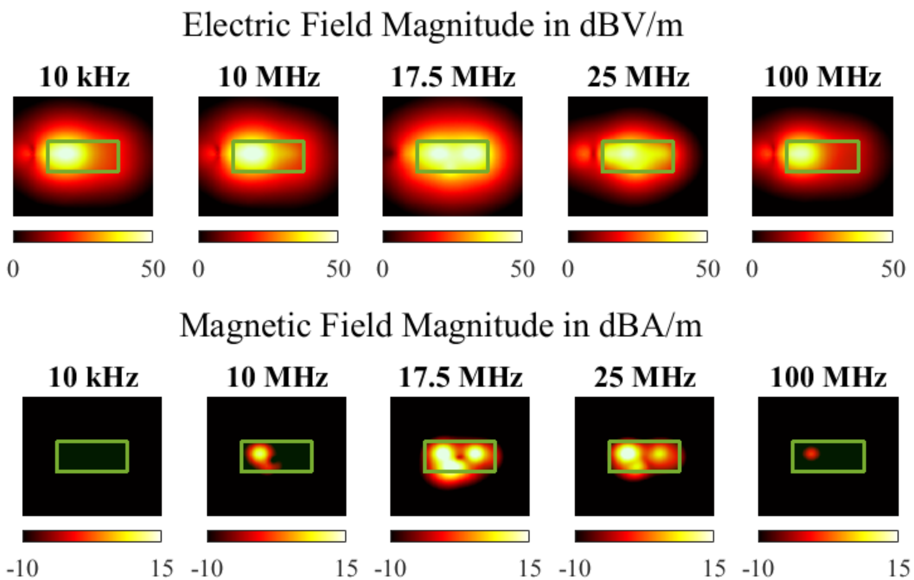

Figure: Near-field simulation results collected 1 cm above the circuit in a 10 cm $\times$ 10 cm plane for the bandpass filter second variant.

Reminder:

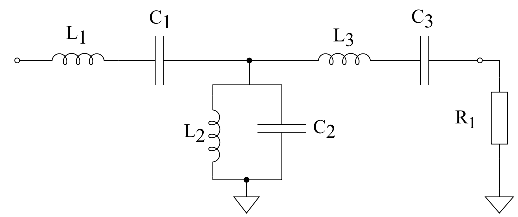

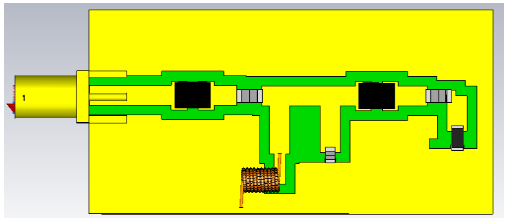

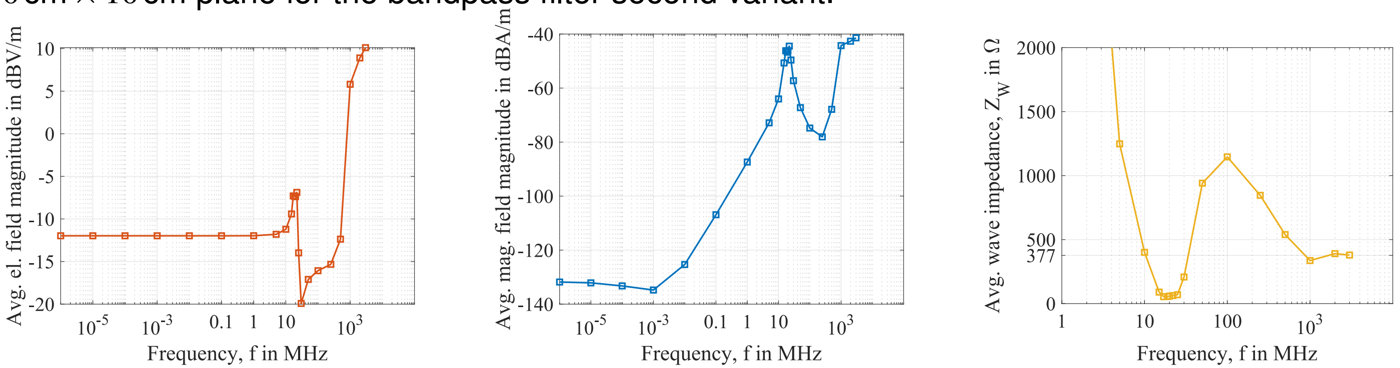

Figure: Average field magnitudes and wave impedance collected 3 cm above the circuit in a 40 cm $\times$ 40 cm plane.

Lumped Wilkinson Divider

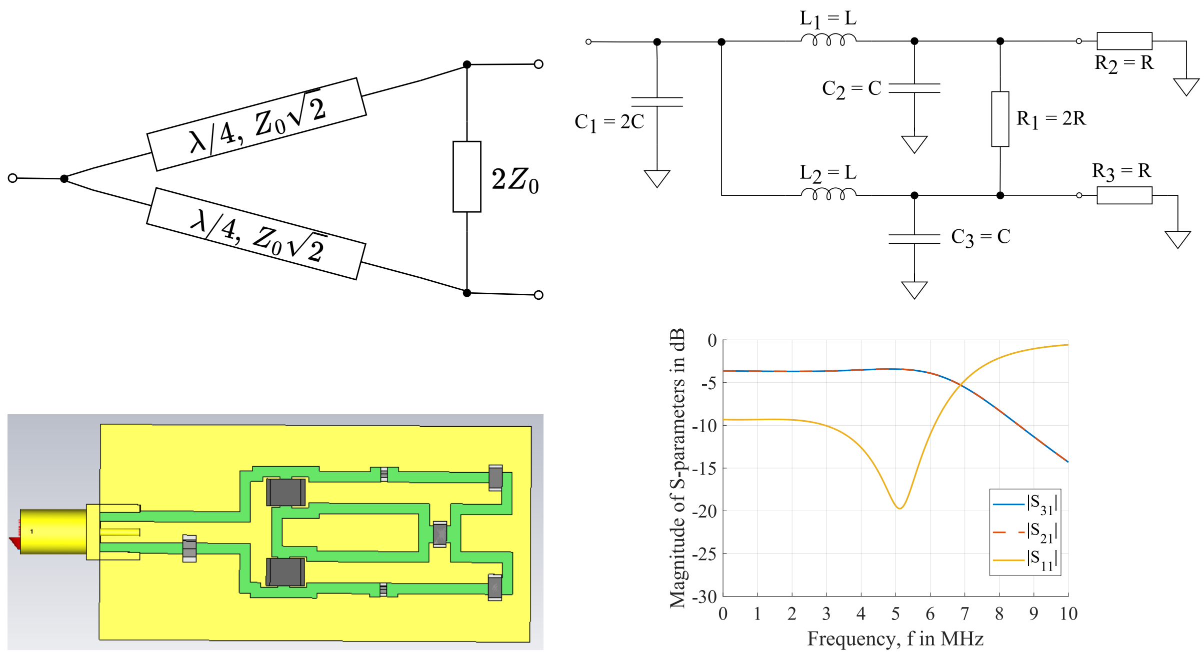

Figure: Distributed implementation (top-left), lumped implementation (top-right). Implemented lumped Wilkinson divider in CST (bottom-left) and its important S-parameters (bottom-right).

$L = Z_0/\omega_0$ and $C = 1/(Z_0\omega_0)$[18]

For this circuit, $Z_0 = 50\,\Omega$, $L = 2.2\,\mu$H and $C = 440\,$pF, thus $L_1 = L_2 = 2.2\,\mu$H, $C_2 = C_3 = 440\,$pF, $C_1 = 1\,$nF, after rounding to the closest standard values.

Lumped Wilkinson Divider

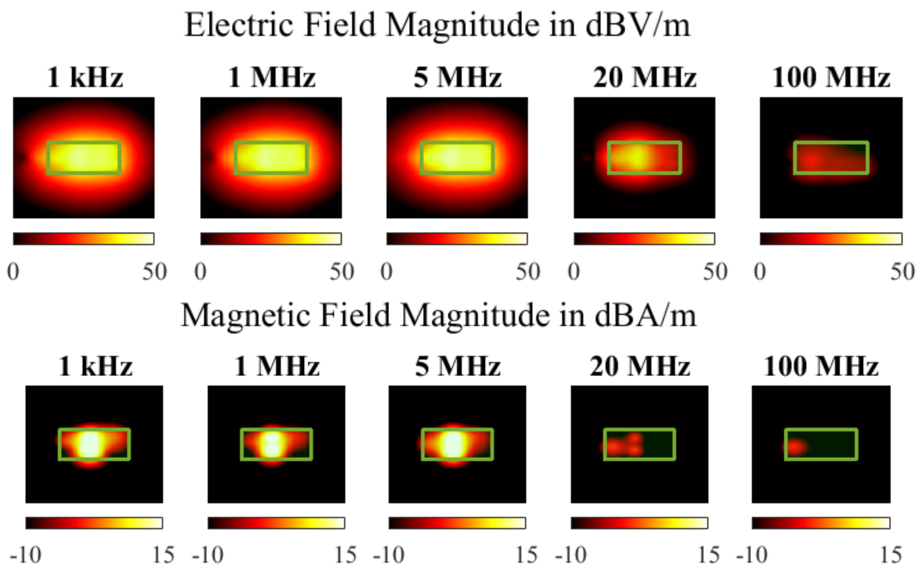

Reminder:

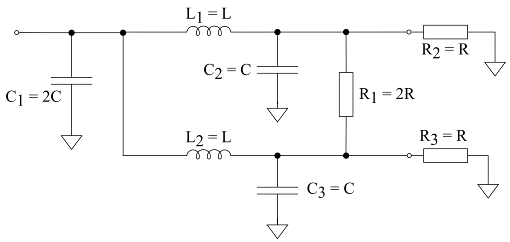

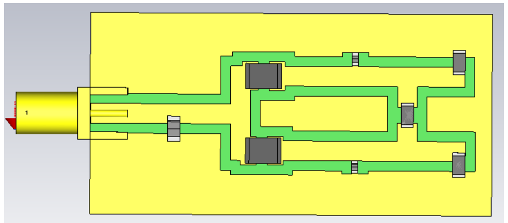

Figure: Near-field simulation results collected 1 cm above the circuit in a 10 cm × 10 cm plane for the Wilkinson divider.

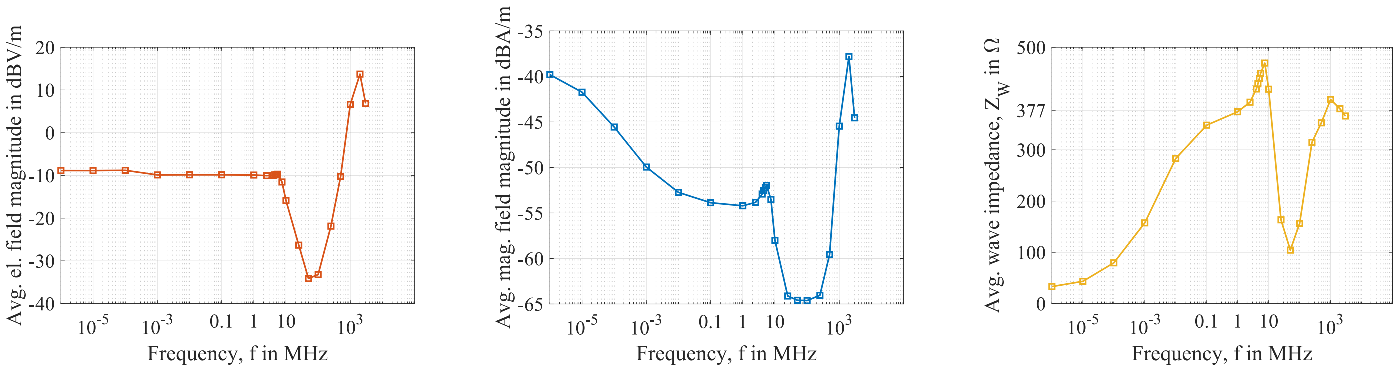

Figure: Average field magnitudes and wave impedance collected 3 cm above the circuit in a 40 cm × 40 cm plane.

Conclusion

In this work the design and implementation of various test circuits with different near-field patterns in CST to test an inverse source solver at low frequencies.

In the first part of the work, the theory of SMD components that are used to implement some of these circuits was presented which includes drum core inductors, air core inductors, multilayer ceramic capacitors and chip resistor.

In the second part of the work the test circuits are implemented which include loop circuits with dominant magnetic field at low frequencies, microstrip circuits with dominant electric field at low frequencies, and the coplanar circuit that has both fields at low frequencies. In addition, basic resonant circuits including bandpass filters, Wilkinson dividers, and hybrid couplers, are implemented of which two bandpass filters and one divider is examined in detail.

References I

[1] N. Gunalp and A. Ozet, “Two-dimensional electromagnetic inverse scattering solutions by a sine-basis moment method,” in *Proceedings of MELECON '94. Mediterranean Electrotechnical Conference*, 1994, 442–445 vol.2. DOI: `10.1109/MELCON.1994.381063`.

[2] T. F. Eibert and C. H. Schmidt, “Multilevel fast multipole accelerated inverse equivalent current method employing rao–wilton–glisson discretization of electric and magnetic surface currents,” *IEEE Transactions on Antennas and Propagation*, vol. 57, no. 4, pp. 1178–1185, 2009. DOI: `10.1109/TAP.2009.2015828`.

[3] U. M. Gür and O. Ergül, “Low-frequency breakdown of the potential integral equations and its remedy,” in *2017 Progress in Electromagnetics Research Symposium - Fall (PIERS - FALL)*, 2017, pp. 676–682. DOI: `10.1109/PIERS-FALL.2017.8293221`.

[4] H. Nagaoka, “The inductance coefficients of solenoids,” *The Journal of the College of Science, Imperial University of Tokyo, Japan*, vol. 27, pp. 1–33, 1909. [Online]. Available: `https://api.semanticscholar.org/CorpusID:107364631`.

[5] E. Rosa and F. Grover, *Formulas and Tables for the Calculation of Mutual and Self-inductance* (Scientific papers of the Bureau of Standards). U.S. Government Printing Office, 1948.

[6] R. G. Medhurst, “H.F. resistance and self-capacitance of single-layer solenoids,” *Wireless Engineer*, vol. 24, pp. 35–43, 80–92, 1947.

References II

[7] E. C. Snelling, *Soft Ferrites: Properties and Applications*, 1st edition. London: Iliffe, 1969, ISBN: 0592027902.

[8] L. Landau and E. Lifschitz, "3 - on the theory of the dispersion of magnetic permeability in ferromagnetic bodies reprinted from physikalische zeitschrift der sowjetunion 8, part 2, 153, 1935.," in *Perspectives in Theoretical Physics*, L. Pitaevski, Ed., Amsterdam: Pergamon, 1992, pp. 51–65, ISBN: 978-0-08-036364-6. DOI: https://doi.org/10.1016/B978-0-08-036364-6.50008-9. [Online]. Available: https://www.sciencedirect.com/science/article/pii/B9780080363646500089.

[9] T. Tsutaoka, "Frequency dispersion of complex permeability in Mn–Zn and Ni–Zn spinel ferrites and their composite materials," *Journal of Applied Physics*, vol. 93, no. 5, pp. 2789–2796, Mar. 2003, ISSN: 0021-8979. DOI: 10.1063/1.1542651. eprint: https://pubs.aip.org/aip/jap/article-pdf/93/5/2789/19266304/2789_1_online.pdf. [Online]. Available: https://doi.org/10.1063/1.1542651.

[10] R. Dosoudil, M. Usakova, E. Usak, and V. Jancarik, "The dispersion characteristics of the complex permeability of nizncu ferrite and its composite materials," *Advances in Electrical and Electronic Engineering*, vol. 3, no. 2, 2011, ISSN: 1804-3119. [Online]. Available: http://advances.utc.sk/index.php/AEEE/article/view/423.

References III

[11] J. Martinez, S. Babic, and C. Akyel, “On evaluation of inductance, dc resistance, and capacitance of coaxial inductors at low frequencies,” *IEEE Transactions on Magnetics*, vol. 50, no. 7, pp. 1–12, 2014. DOI: 10.1109/TMAG.2014.2303943.

[12] F. Grover, *Inductance Calculations* (Dover Books on Electrical Engineering). Dover Publications, 2013, ISBN: 9780486318356. [Online]. Available: https://books.google.de/books?id=H4LCAgAAQBAJ.

[13] Y. Cheng and Y. Shu, “A new analytical calculation of the mutual inductance of the coaxial spiral rectangular coils,” *IEEE Transactions on Magnetics*, vol. 50, no. 4, pp. 1–6, 2014. DOI: 10.1109/TMAG.2013.2290972.

[14] M.-J. Pan and C. A. Randall, “A brief introduction to ceramic capacitors,” *IEEE Electrical Insulation Magazine*, vol. 26, no. 3, pp. 44–50, 2010. DOI: 10.1109/MEI.2010.5482787.

[15] A. Asmanis, D. Stepins, A. Dzenis, and G. Asmanis, “3d modeling of surface-mount capacitors and mutual couplings between them,” in *2017 International Symposium on Electromagnetic Compatibility - EMC EUROPE*, 2017, pp. 1–6. DOI: 10.1109/EMCEurope.2017.8094717.

[16] U. Siart, “Einführung in die Hochfrequenztechnik,” German, Lecture notes, Technical University of Munich, 2020.

[17] H. Y.-F. Lam, *Analog and Digital Filters: Design and Realization*. Englewood Cliffs, N.J.: Prentice-Hall, 1979, ISBN: 0-13-032755-7.

References IV

[18] F. Wang and H. Wang, “A high-power broadband multi-primary dat-based doherty power amplifier for mm-wave 5g applications,” *IEEE Journal of Solid-State Circuits*, vol. 56, no. 6, pp. 1668–1681, 2021. DOI: 10.1109/JSSC.2021.3070800.